

Deep-sub-cycle attosecond optical pulses

Hongliang Dang,¹⁺ Jiaxin Gao,¹⁺ Hao Wu,¹ Xin Guo,¹ Y. R. Shen,² Limin Tong^{1,*}

¹New Cornerstone Science Laboratory, Interdisciplinary Center for Quantum Information, State Key Laboratory of Extreme Photonics and Instrumentation, College of Optical Science and Engineering, Zhejiang University, Hangzhou 310027, China

²Physics Department, University of California at Berkeley, Berkeley, California 94720, USA

⁺These authors contribute equally.

* Corresponding author: phytong@zju.edu.cn

Abstract

Sub-cycle optical pulse is of great importance for ultrafast science and technology. While a narrower pulse can offer a higher temporal resolution, so far the pulse width has not exceeded the limit of half an optical cycle. Here we propose to break the half-cycle limit via inverse Compton scattering in a nano-slit optical mode, in which a deep-subwavelength-confined optical field can be converted into a deep-sub-cycle attosecond pulse by high-speed free electrons flying through. Our calculations show that, with experimentally reachable conditions, a measurable deep-sub-cycle attosecond pulse with a width narrower than half an optical cycle can be generated. Quantitatively, using a deep-subwavelength-confined 4.4- μm -wavelength 100-fs pulsed optical driving field and a 2-MeV 50-as 5-pC electron bunch, we obtain an attosecond pulse with a peak frequency of 2.55 PHz, a pulse width of 99 as (~ 0.25 optical cycle), and a single-pulse photon number larger than 200 around the material damage threshold. Such pulses may open opportunities for studying light-matter interaction on the deep-sub-cycle level, and pave a way to unprecedented optical technology ranging from temporal super-resolution optical microscopy and spectroscopy to unconventional atom/molecule polarization and manipulation.

Space and time are basic scales for understanding the world. Higher spatial (e.g., from optical[1,2] to electron microscopy[3,4]) and temporal (e.g., from femtosecond[5,6] to attosecond[7,8] technology) resolutions are always desired for a better understanding of the microscopic world on a deeper level[5,8]. On the temporal scale, so far the highest resolution comes from ultrafast optical technology, which has been widely employed for studying the dynamics of molecular or atomic processes from femtosecond to attosecond scales[3,5-10]. Typically, to pursue a higher temporal resolution, we have to resort to shorter optical pulses with higher photon energy (i.e., shorter wavelength), which is analogous to achieving higher diffraction-limited spatial resolution by reducing the wavelength of the probing light (e.g., X-ray microscopy[11]). However, as we know now, a more effective way to increase the spatial resolution and resolve the sub-diffraction structure is not by reducing the wavelength, but by confining the light field to a spatial scale well below the half wavelength (i.e., deep-subwavelength scale) that breaks the optical diffraction limit in the near field, and obtain a super-diffraction-limit optical resolution at the frequency not much far away from the concerned resonance of the material, such as optical near-field microscopy [1,12,13]. Compared with the spatial super-resolution technology that has been well recognized and developed, the temporal super-resolution remains challenging, due to the absence of the deep-sub-cycle optical field with a pulse width shorter than half a cycle.

In recent years, various approaches[14-21] based on e.g., optical parametric chirped pulse amplification (OPCPA)[14,15], optical arbitrary waveform generation (OAWG)[16,17], and relativistic electron sheet (RES)[18,19], have been developed to generate sub-cycle ultrafast optical pulses. However, due to difficulties such as limited gain

bandwidth of femtosecond laser sources[20] and insufficient degree of freedom of waveform control[21], the narrowest pulse width obtained remains larger than $T_c/2$ ($T_c/2$ on the temporal scale is analogous to the diffraction limit of $\lambda/2$ on the spatial scale, where T_c and λ are the cycle and the wavelength of the light).

Here, we propose to generate deep-sub-cycle ultrafast optical pulses via inverse Compton scattering (ICS) in a nano-slit optical mode, in which a deep-sub-wavelength-confined optical field with a spatial full width at half maximum (FWHM_s) smaller than the half wavelength is converted into a deep-sub-cycle optical pulse via ICS by high-speed electrons flying through.

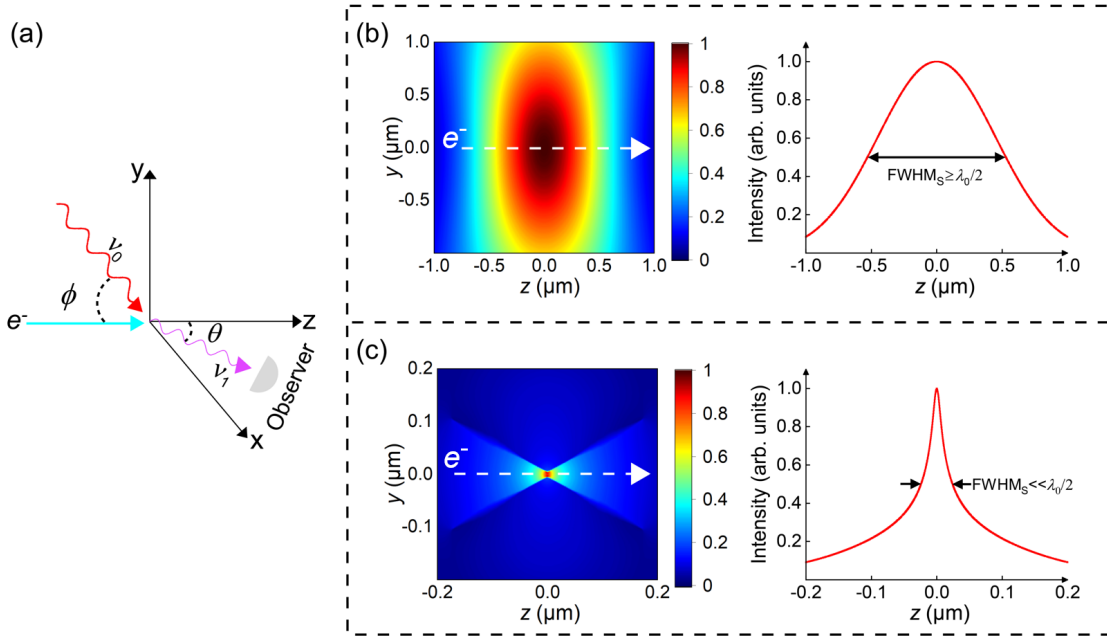


FIG. 1. Schematic illustration of breaking the half-cycle temporal limit of an optical pulse. (a) Inverse Compton scatter (ICS) between a photon and a high-speed electron. Typically, the electron energy is much higher than the initial photon energy, and the photon energy will be increased after ICS (i.e., $\nu_1 > \nu_0$), while the energy loss of the electron is negligible. (b) Calculated field intensity distribution (left panel) and FWHMs (right panel) of a conventional Gaussian-profile 1.8- μm -wavelength optical field that is focused approaching the diffraction limit. Due to the diffraction limit, the FWHMs cannot be smaller than $\lambda_0/2$, which sets the lower limit of the transition time (τ_1) to be larger than half an optical cycle when an electron flies through. (c) Calculated field intensity distribution (left panel) and FWHMs (right panel) of a deep-sub-wavelength confined optical field. Here the FWHMs can be much smaller than $\lambda_0/2$, making it possible to decrease τ_1 well below half an optical cycle, and generate a deep-sub-cycle optical pulse that breaks the half-cycle temporal limit.

Our approach to breaking the half-cycle limit of an optical pulse is illustrated in Fig.1. In the laboratory coordinate system, when a photon (with a frequency ν_0 and wavelength λ_0) collides with an electron with much higher energy (e.g., a free-space high-speed electron), it can be converted into a photon with higher energy (i.e., a higher frequency ν_1 and a shorter wavelength λ_1) by ICS (Fig. 1a; see also section I in Supplemental Material). Usually, the photon is provided by a focused laser beam in free space with a spot size larger than the diffraction limit (Fig. 1b), as has been reported in previous works[22-24]. When an electron with a velocity V_e flies through the focused optical field with a Gaussian-profile intensity distribution (FWHM_s $\geq \lambda_0/2$), the scattered photons will compose a virtual pulse (compared to a typical pulse that usually contains a large number of photons, the single-electron-scattered pulse typically has an average photon number much less than 1, and is thus called a “virtual” pulse here) with a width τ_1 that can be estimated by

$$\tau_1 \approx \left(\frac{\text{FWHM}_s}{V_e} \right) \cdot (1 - \beta \cos \theta) \quad (1)$$

where θ is the emission angle (see Fig. 1a), $\beta = V_e/c$, and the factor $(1 - \beta \cos \theta)$ comes from the time compression effect for the observer facing the scattered photon [25]. Since $\lambda_1 = \lambda_0 \cdot (1 - \beta \cos \theta)$ (see section I in Supplemental Material), $V_e < c$, we have $\tau_1 > \lambda_1/2c = T_{c1}/2$, showing that the width of a pulse composed of conventional ICS photons can hardly be shorter than the half-cycle limit $T_{c1}/2$.

Recently, a deep-sub-wavelength-confined optical field has been realized in a nano-slit waveguide mode [26-29], which can offer a high-intensity peak field with $\text{FWHM}_s \ll \lambda_0/2$ at the center of the mode in the optical near field (Fig. 1c; see also section III in Supplemental Material), and a low-intensity diffraction-limited background field with a large peak-to-background ratio. When an electron flies through such a field, a deep-sub-cycle virtual pulse can be obtained with a temporal width $\tau_1 < T_{c1}/2$ providing that $V_e > 2c \cdot \text{FWHM}_s/\lambda_0$. For example, if $\text{FWHM}_s/\lambda_0 = 1/4$, to have $\tau_1 < T_{c1}/2$, the electron should have $V_e > 0.5c$, which can be readily achieved by relatively small electron acceleration systems (e.g., an electron microscope [30]).

For principle exploration, we first consider the simplest case with single-electron incidence. We assume that the wavelength of the pulsed optical driving field (λ_0) is 1.8 μm (a common wavelength of the driving field in high harmonic generation (HHG)[31,32]), and the field is confined as a nano-slit waveguide mode formed by coupling two identical CdS single-crystal nanowires (i.e., a coupled nanowire pair, CNP, see Fig. 2a)[26,27]. By assuming a slit width of 20 nm and a nanowire diameter of 500 nm, we have a $\text{FWHM}_s \sim 77$ nm (corresponding to a $\text{FWHM}_s/\lambda_0 \sim 0.043$) of the central peak along the z -direction (Fig. 2b). Meanwhile, we assume that the electron has a kinetic energy of 1 MeV (corresponding to a velocity $V_e \sim 0.94c$), and flies through the confined optical field from left to right along the central symmetry line (i.e., the z -direction) of the CNP cross-section (Fig. 2a). Due to the symmetry of the CNP structure and thus that of the optical driving field, the electron collides with photons almost perpendicularly on their motion trajectories (i.e., $\phi = \pi/2$ in Fig. 1a). In such a case, the path-dependent (i.e., z -dependent) scattered photon number $n(z)$ can be obtained as (see also section IV in Supplemental Material for details)[22]

$$n(z) = N_0 N_e \sigma_T \frac{S(z)}{P_{\text{mode}}} \frac{\delta_t}{\tau_0} \quad (2)$$

where the total photon number of the driving field $N_0 \approx E_{p0}/h\nu_0$, in which E_{p0} is the total energy of the driving pulse, h is the Planck constant, and ν_0 the central frequency of the driving pulse; N_e is the number of incident electrons (here $N_e = 1$), σ_T is the Thomson scattering cross section ($\sigma_T = 6.65 \times 10^{-29} \text{ m}^2$), $S(z)$ is the z -dependent Poynting vector, P_{mode} is the mode power (i.e., the mode area integral of Poynting vector) of the optical driving field at the moment the electron flying through, δ_t is the transition time of the electron, and τ_0 is the width of the driving pulse (with an assumption of $\tau_0 > \delta_t$). Since δ_t (typically tens to hundreds of attoseconds) is much shorter than τ_0 (typically tens to hundreds of femtoseconds), P_{mode} is almost a constant during the time of electron transit, and can be assumed as the average power of the pulsed driving field (i.e., $P_{\text{mode}} = E_{p0}/\tau_0$).

When the electron flies through the driving field along the z -direction (Fig. 2b), due to the negligible energy loss of the electron compared with its initial energy (i.e., 1 MeV), V_e can be assumed as a constant (i.e., $V_e \sim 0.94c$) and the trajectory of the electron is almost a straight line (see also section VI in Supplemental Material for details). When we assume a spherical receiving surface centered on the center of the nano-slit (i.e., at $y=z=0$, see also Fig.S1), or equivalently

a concave mirror group to guide the scattered photons out (Fig.2a), in the laboratory coordinate system, the angular distribution of the scattered photons $n(z)$ can be described by a factor $f(\theta)$, and the number of scattered photons received at time t and angle θ can be approximately obtained as[22]

$$n(t, \theta) = n(z) \cdot f(\theta), \quad (3)$$

where the path-dependence (i.e., z -dependence) is converted to the time-dependence (i.e., t -dependence) by $t = z \cdot (1 - \beta \cos \theta) / V_e$, and $f(\theta) = K \cdot \chi^2 (1 + 2\chi(\chi - 1))$ [22], in which K is a constant coefficient and $\chi = 1 / (1 + \theta^2 / (1 + \beta^2))$.

Correspondingly, the intensity of the ICS pulse at time t and angle θ can be obtained as

$$I(t, \theta) = n(t, \theta) \cdot h\nu, \quad (4)$$

where $\nu = v_0 / (1 - \beta \cos \theta)$.

By integrating over all possible θ , we obtain the temporal profile of the virtual pulse (i.e., $I(t)$) with a temporal full width at half maximum (FWHM_T) of 19 as (Fig. 2c, see also section V in Supplemental Material), which is much narrower than that of an ICS pulse generated with the same electron but a 1.8- μm -wavelength diffraction-limited driving field with a Gaussian-profile intensity distribution (red dotted line in Fig.2c).

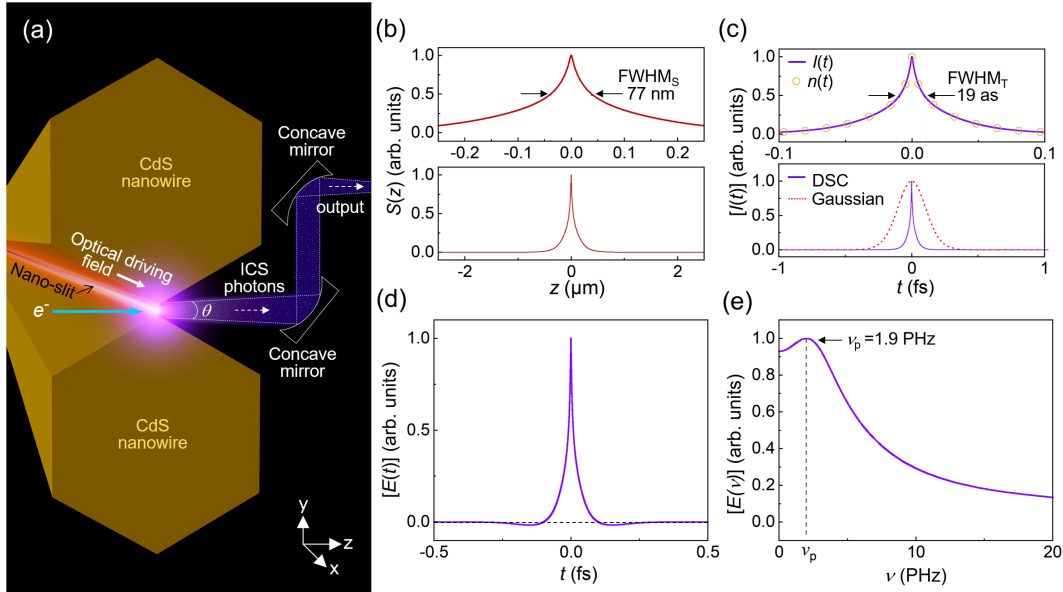


FIG. 2. Generation of deep-sub-cycle optical pulses with single-electron incidence. (a) Schematic diagram of the ICS system. An electron incident from the left side collides perpendicularly with photons in a confined optical driving field, which is generated along a nano-slit between two coupled CdS nanowires. (b) Normalized z -axis Poynting vector of an optical driving field, generated with a slit size of 20 nm, a nanowire diameter of 500 nm and a wavelength of 1.8 μm . The close-up image (upper panel) shows the extremely confined field with a FWHM_S of 77 nm. (c) $I(t)$ of the virtual ICS pulse, giving a FWHM_T of 19 as (upper panel). For reference, photon numbers $n(t)$ is also provided (orange circle), which basically overlaps with $I(t)$. For comparison, $I(t)$ of a virtual ICS pulse generated in a Gaussian-profile optical driving field is also provided (red dotted line, lower panel). DSC: deep-sub-cycle pulse, Gaussian: Gaussian-profile pulse. (d) $E_y(t)$ of the DSC pulse in (c). (e) Fourier spectrum $E(\nu)$ of the pulse in (d), giving a peak frequency of ~ 1.9 PHz.

Since the phase of the scattered field is inherited from the optical driving field[33], to maximize the peak intensity of the ICS pulse, we assume that the amplitude of the driving field reaches the positive maximum when the electron

arrives at the central point of the nano-slit (i.e., $z=0$). Thus, in the spatial far field, the transverse scattered electric field $E_y(t)$ can be obtained as

$$E_y(t, \theta) = \sqrt{2 \sqrt{\frac{\mu_0}{\epsilon_0}} \cdot I(t, \theta) e^{i2\pi\nu_0 \left(\frac{t}{1-\beta\cos\theta}\right)}}, \quad (5)$$

where ϵ_0 and μ_0 are the vacuum permittivity and the magnetic permeability, respectively. By integrating over all possible θ , we obtain $E_y(t)$ shown in Fig. 2d, which agrees well with the classical radiation model of an arbitrarily accelerated electron (see section VII in Supplemental Material). Unlike the conventional dipolar pulses, here the central part with significant amplitude of the pulse is mainly generated by the unidirectional acceleration of the electron driven by the optical driving field (see section VI in Supplemental Material), and is thus a unipolar pulse with non-zero electric area [34-37]. Fig. 2e gives the Fourier spectrum of such a virtual pulse, revealing a peak frequency ν_p of 1.9 PHz (corresponding to a $T_{c1} \sim 0.52$ fs). After the peak frequency ν_p , the amplitude of $E(\nu)$ decreases quickly with increasing frequency. Since FWHM_T (19 as) is much shorter than a half cycle at the peak frequency (i.e., 0.26 fs at 1.9 PHz), such an ICS-generated pulse is a virtual deep-sub-cycle pulse.

It is worth mentioning that, compared with the temporal profiles of previously reported ultrafast sub-cycle [14-21] or multiple-cycle pulses [14,16,22], here the deep-sub-cycle pulse has a spike-like profile much sharper at the center, which enables a much tighter confinement on the temporal scale. For ease of comparison, we define a temporal confinement factor $\zeta = T_{c1}/\tau_1$, in which $\zeta > 2$ sets a deep-sub-cycle criterion that breaks the conventional half-cycle temporal confinement limit. For example, for the virtual pulse mentioned above, the calculated $\zeta \sim 27$.

Using single-electron incidence (i.e., $N_e=1$), the number of ICS-generated photons in a single pulse ($N_{SP} = \int n(t)dt$) is too low ($N_{SP} \ll 1$) to compose an experimentally measurable pulse. For reference, when using a power density of the optical driving field approaching the damage threshold of the CdS crystal ($\sim 1.7 \times 10^{16}$ W/m² [38,39]) at the nano-slit edge, the calculated $N_{SP} \sim 2.5 \times 10^{-8}$. For practical application, N_{SP} should be much larger than 1. To increase N_{SP} , we propose to use a high-density electron bunch [40-44] (i.e., increase the electron number), optical material with a higher optical damage threshold to construct the CNP (i.e., increase the power density of the optical driving field), driving field with a longer wavelength and thus a larger slit size (i.e., increase the ICS volume and thus the electron and photon numbers involved). Meanwhile, to compensate the temporal broadening of the ICS pulse due to the enlarged slit size, as well as to obtain a high density of the electron bunch, we use an electron bunch with higher speed. Specifically, we use the following experimentally reachable parameters: (1) an electron bunch with a duration of 50 as, an electron charge of 5 pC (corresponding to an electron density of 1.3×10^{28} /m³), an electron energy of 2 MeV, and an elliptical cross-section; (2) a pulsed driving field with a central wavelength of 4.4 μm and a pulse width of 100 fs [45]; (3) a CNP consisted of two identical sapphire hexagonal prisms, with a diagonal diameter of 1.2 μm , a slit size of 200 nm (corresponding to a FWHM_S of 808 nm), and a peak power density of 1.3×10^{18} W/m² at the center of the nano-slit (see section VIII in Supplementary Materials) that keeps the power density at the inner edge of the slit below the optical damage threshold of 2×10^{18} W/m² of the sapphire [46] (over two orders magnitude higher than that of the CdS). In addition, similar to the single-electron-incidence case, the energy loss of the focused electron bunch is negligible during the ICS process.

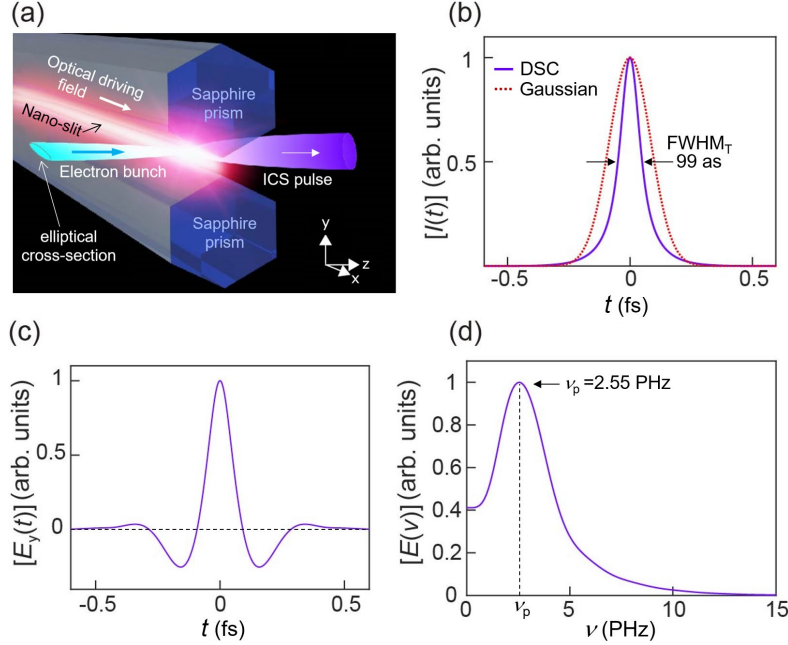


FIG. 3. Generation of deep-sub-cycle optical pulses with an ultrafast electron-bunch pulse. (a) Schematic diagram of the ICS system. A focused electron bunch with an elliptical cross-section is incident from the left side of a nano-slit, collides with photons in the confined optical driving field that is generated along the nano-slit between two coupled sapphire prisms. (b) $I(t)$ of the ICS pulse, generated via ICS of a 50-as 2-MeV electron bunch in a pulsed driving field with a FWHMs of 808 nm, a wavelength of 4.4 μm and a pulse width of 100 fs. The measured pulse width (FWHM_T) is 99 as. For comparison, $I(t)$ of an ICS pulse generated in a 4.4- μm -wavelength Gaussian-profile optical driving field is also provided (red dotted line). DSC: deep-sub-cycle pulse, Gaussian: Gaussian-profile pulse. (c) $E_y(t)$ of the DSC pulse in (b). (d) Fourier spectrum $E(v)$ of the pulse in (c), giving a peak frequency of ~ 2.55 PHz.

With the above-mentioned assumptions, we obtained an ICS pulse shown in Fig. 3b, which is composed of a series of single-electron-incidence sub-pulses (see section V in Supplemental Material). Owing to the significantly increased electron number (from $N_e=1$ to 3.1×10^7) and driving-field photon number, the photon number of the ICS pulse is increased to 269, an experimentally measurable level. Broadened by the temporal distribution of electrons (i.e., $\tau_e=50$ as), the temporal profile is no longer sharp-spike like. However, the overall ICS-pulse width τ_1 (i.e., FWHM_T) of 99 as, remains much narrower than that of an ICS pulse generated with the same electron bunch but a 4.4- μm -wavelength diffraction-limited driving field with a Gaussian-profile intensity distribution (red dotted line in Fig.3b). Fig. 3c gives calculated $E_y(t)$ of the ICS pulse shown in Fig. 3b, which retains the unipolar feature of single-electron-incidence ICS pulse (Fig.2d). Fig.3d gives $E(v)$, the Fourier transform of the $E_y(t)$ in Fig. 3c, revealing a peak frequency ν_p of 2.55 PHz (corresponding to a $T_{c1} \sim 0.39$ fs), which is much higher than that in Fig.2e (i.e., 1.9 PHz) due to the much higher electron energy (2 MeV v.s. 1 MeV).

Despite the broadening of τ_1 , calculated $\zeta(T_{c1}/\tau_1=4.0)$ remains much larger than 2. Meanwhile, the fraction of photon numbers within the FWHM_T ($N_{\text{SP_FWHM}}/N_{\text{SP}}$) is about 0.60, which is lower than 0.76 of a conventional Gaussian-profile pulse. Also, when a high-repetition-rate (e.g., 100 kHz) ultrafast pulses are used to generate both the electron bunch and the optical driving field, the photon flux (i.e., brightness) of the deep-sub-cycle ICS pulses can reach a considerable value (e.g., $\sim 10^8$ photons per second). Overall, these results show that ICS using a high-speed high-density electron bunch and a deep-sub-wavelength confined optical driving field is highly promising for generating isolated deep-sub-cycle attosecond optical pulses.

Compared with existing methods for sub-cycle ultrafast pulse generation (e.g., OPCPA, OAWG and RES) that have not yet exceeded the half-cycle limit, our approach proposed here can break the half-cycle limit and achieve deep-sub-cycle pulses with $\zeta > 2$ (see section IX in Supplemental Material), while maintaining a stable carrier envelope when it propagates to the far field (see section X in Supplemental Material). Meanwhile, by using different parameter combinations of electron bunch and CNP, more possibilities for generating deep-sub-cycle pulses can be explored. For example, by using sapphire microfibers (with circular cross-sections) instead of sapphire prism (with hexagonal cross-sections) while retaining other parameters (Fig.4a), N_{SP} is increased from 269 (in Fig.3b) to 370 (in Fig.4b), benefitting from a higher allowed peak power density (1.9×10^{18} W/m²) at the center of the nano-slit (Fig. 4a). Meanwhile, owing to a larger fraction of mode power confined within the FWHMs region, τ_1 decreases from 99 as to 91 as, resulting in an increase of ζ from 4.0 to 4.3.

Also, by changing the wavelength (i.e., λ_0) and/or the confinement (i.e., FWHMs) of the optical driving field, it is possible to change ζ within a wide range. Figure 4c gives the dependence of ζ on λ_0 and FWHMs of the driving field, with the same electron bunch used in Fig.3 (i.e., pulse width of 50 as, electron energy of 2 MeV). It shows that, with λ_0 increased from 1 to 5 μ m, ζ can be increased from ~ 1 to larger than 5. With the same λ_0 , ζ can be increased by reducing FWHMs. However, with increasing ζ , N_{SP} decreases (Fig.4d). For reference, when ζ is increased to from 4.0 to 4.2, N_{SP} decreases quickly from 269 to 128. On the other hand, using a decreased ζ (e.g., using a larger slit width and thus a larger FWHMs), N_{SP} can be increased significantly. For example, when ζ is decreased to 3.2 (still larger than 2), N_{SP} can be increased to 1260. Therefore, for practical applications, a trade-off between ζ and N_{SP} should be considered.

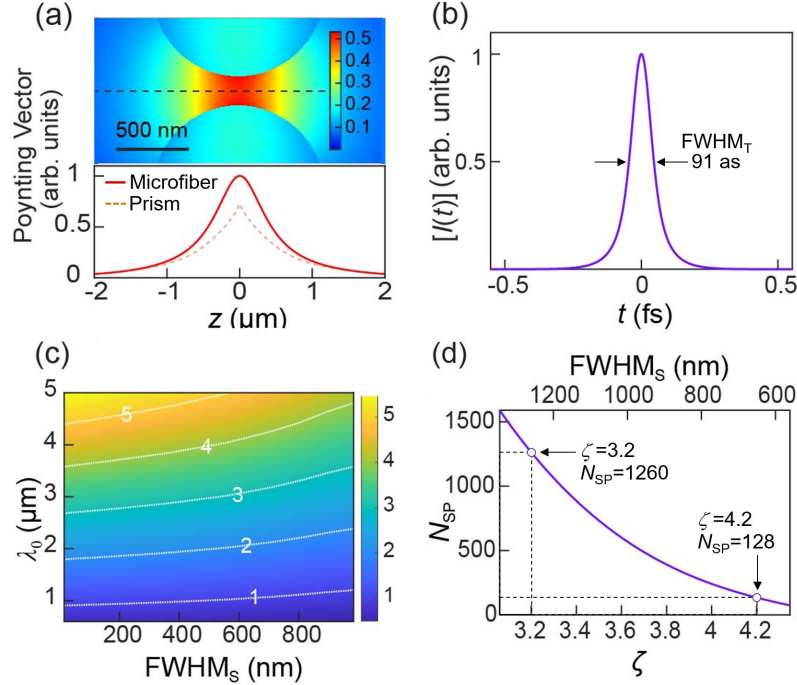


FIG. 4. Generation of deep-sub-cycle optical pulses with more possibilities. (a) Normalized z -axis Poynting vector of an optical driving field generated in two coupled sapphire microfibers, calculated with a microfiber diameter of 1.2 μ m, a slit size of 200 nm and a wavelength of 4.4 μ m. For comparison, Poynting vector of an optical driving field generated in two coupled sapphire prisms in Fig.3 is also provided (orange dashed line, lower panel). (b) $I(t)$ of the ICS pulse generated via ICS of a 50-as 2-MeV electron bunch in the driving field in (a), giving a pulse width (FWHM_T) of 91 as. (c) Dependence of ζ on FWHMs and λ_0 of the optical driving field generated in two coupled sapphire prisms in Fig.3, with a 50-as 2-MeV electron bunch. (d) Dependence of N_{SP} on ζ and FWHMs, with an optical driving field of 4.4- μ m wavelength and a 1.9×10^{18} W/m² peak power density, and a 50-as 2-MeV 5-pC electron bunch.

In conclusion, so far we have demonstrated an approach to generating a deep-sub-cycle ultrafast optical pulse based on ICS between high-speed electrons and a deep-sub-wavelength confined optical driving field. We show that, with reachable experimental conditions, it is possible to obtain single attosecond optical pulse with width shorter than a half optical cycle, which has not yet been achieved by other means. As dipolar/multipolar oscillation in optical polarization or resonance is, in general, the underlying mechanism of light-matter interaction[47], and the half-cycle pulse width is the temporal limit of the current ultrafast optical pulses [36,48], the deep-sub-cycle optical pulse demonstrated here can not only break the half-cycle limit and reveal deep-sub-cycle dynamics in light-matter interaction, but can also be used to manipulate (e.g., excite or mediate) optical response on the deep-sub-cycle level and generate previously difficult-to-reach or unreachable processes (e.g., non-dipole photoionization[49], anharmonic or temporal dark-mode states). Overall, the results demonstrated here proposed an approach to deep-sub-cycle ultrafast optical pulses, which may open opportunity for studying light-matter interaction on a deep-sub-cycle temporal scale, and pave a way to temporal super-resolution optical technology ranging from deep-sub-cycle ultrafast microscopy, spectroscopy to atom/molecule manipulation.

Acknowledgements

This work was supported by New Cornerstone Science Foundation (NCI202216) and National Natural Science Foundation of China (62175213, 92150302).

References

- [1] E. Betzig, J. K. Trautman, T. D. Harris, J. S. Weiner, and R. L. Kostelak, "Breaking the diffraction barrier: optical microscopy on a nanometric scale," *Science* **251**, 1468-1470 (1991).
- [2] S. W. Hell *et al.*, "The 2015 super-resolution microscopy roadmap," *J. Phys. D: Appl. Phys.* **48**, 443001 (2015).
- [3] A. H. Zewail, "Four-dimensional electron microscopy," *Science* **328**, 187-193 (2010).
- [4] R. F. Egerton and M. Watanabe, "Spatial resolution in transmission electron microscopy," *Micron* **160**, 103304 (2022).
- [5] A. H. Zewail, "Femtochemistry: atomic-scale dynamics of the chemical bond," *The Journal of Physical Chemistry A* **104**, 5660-5694 (2000).
- [6] A. Stolow, A. E. Bragg, and D. M. Neumark, "Femtosecond time-resolved photoelectron spectroscopy," *Chem. Rev.* **104**, 1719-1758 (2004).
- [7] P. B. Corkum and F. Krausz, "Attosecond science," *Nat. Phys.* **3**, 381-387 (2007).
- [8] F. Krausz and M. Ivanov, "Attosecond physics," *Rev. Mod. Phys.* **81**, 163-234 (2009).
- [9] J. Itatani, F. Quéré, G. L. Yudin, M. Y. Ivanov, F. Krausz, and P. B. Corkum, "Attosecond streak camera," *Phys. Rev. Lett.* **88**, 173903 (2002).
- [10] D. M. Jonas, "Two-dimensional femtosecond spectroscopy," *Annu. Rev. Phys. Chem.* **54**, 425-463 (2003).
- [11] A. Sakdinawat and D. Attwood, "Nanoscale x-ray imaging," *Nat. Photonics* **4**, 840-848 (2010).
- [12] R. C. Dunn, "Near-field scanning optical microscopy," *Chem. Rev.* **99**, 2891-2928 (1999).
- [13] X. Chen, D. Hu, R. Mescall, G. You, D. N. Basov, Q. Dai, and M. Liu, "Modern scattering-type scanning near-field optical microscopy for advanced material research," *Adv. Mater.* **31**, 1804774 (2019).
- [14] S.-W. Huang *et al.*, "High-energy pulse synthesis with sub-cycle waveform control for strong-field physics," *Nat. Photonics* **5**, 475-479 (2011).
- [15] G. M. Rossi *et al.*, "Sub-cycle millijoule-level parametric waveform synthesizer for attosecond science," *Nat. Photonics* **14**, 629-635 (2020).

- [16] S. T. Cundiff and A. M. Weiner, "Optical arbitrary waveform generation," *Nat. Photonics* **4**, 760-766 (2010).
- [17] N. K. Fontaine, R. P. Scott, L. Zhou, F. M. Soares, J. Heritage, and S. Yoo, "Real-time full-field arbitrary optical waveform measurement," *Nat. Photonics* **4**, 248-254 (2010).
- [18] W. J. Ma *et al.*, "Bright subcycle extreme ultraviolet bursts from a single dense relativistic electron sheet," *Phys. Rev. Lett.* **113**, 235002 (2014).
- [19] E. Siminos, I. Thiele, and C. Olofsson, "Laser wakefield driven generation of isolated carrier-envelope-phase tunable intense subcycle pulses," *Phys. Rev. Lett.* **126**, 044801 (2021).
- [20] C. Manzoni, O. D. Mücke, G. Cirimi, S. Fang, J. Moses, S. W. Huang, K. H. Hong, G. Cerullo, and F. X. Kärtner, "Coherent pulse synthesis: towards sub - cycle optical waveforms," *Laser Photon Rev* **9**, 129-171 (2015).
- [21] C. Manzoni and G. Cerullo, "Design criteria for ultrafast optical parametric amplifiers," *J. Opt.* **18**, 103501 (2016).
- [22] R. W. Schoenlein *et al.*, "Femtosecond x-ray pulses at 0.4 Å generated by 90° Thomson scattering: a tool for probing the structural dynamics of materials," *Science* **274**, 236-238 (1996).
- [23] M. Placidi, S. Di Mitri, C. Pellegrini, and G. Penn, "Compact FEL-driven inverse Compton scattering gamma-ray source," *Nucl. Instrum. Methods Phys. Res., Sect. A* **855**, 55-60 (2017).
- [24] J. Vyskočil, E. Gelfer, and O. Klimo, "Inverse Compton scattering from solid targets irradiated by ultra-short laser pulses in the 1022–1023 W/cm² regime," *Plasma Phys. Controlled Fusion* **62**, 064002 (2020).
- [25] A. Hofmann, *The Physics of Synchrotron Radiation* (Cambridge University Press, Cambridge, 2004), Cambridge Monographs on Particle Physics, Nuclear Physics and Cosmology.
- [26] H. Wu, L. Yang, P. Z. Xu, J. Gong, X. Guo, P. Wang, and L. M. Tong, "Photonic nanolaser with extreme optical field confinement," *Phys. Rev. Lett.* **129**, 013902 (2022).
- [27] L. Yang, Z. K. Zhou, H. Wu, H. L. Dang, Y. X. Yang, J. X. Gao, X. Guo, P. Wang, and L. M. Tong, "Generating a sub-nanometer-confined optical field in a nanoslit waveguiding mode," *Adv. Photonics* **5**, 046003 (2023).
- [28] Y. R. Shen, "Optical waveguiding along nanometer slits," *Adv. Photonics* **5**, 040503 (2023).
- [29] Y. X. Yang, J. X. Gao, H. Wu, Z. K. Zhou, L. Yang, X. Guo, P. Wang, and L. M. Tong, "Generating a nanoscale blade-like optical field in a coupled nanofiber pair," *Photonics Res.* **12**, 154-162 (2024).
- [30] R. K. Li and P. Musumeci, "Single-shot MeV transmission electron microscopy with picosecond temporal resolution," *Phys. Rev. Appl.* **2**, 024003 (2014).
- [31] B. E. Schmidt, A. D. Shiner, C. Trallero-Herrero, H. J. Wörner, S. Patchkovskii, J. C. Kieffer, P. B. Corkum, D. M. Villeneuve, and F. Légaré, in *2011 Conference on Lasers and Electro-Optics Europe and 12th European Quantum Electronics Conference (CLEO EUROPE/EQEC)2011*, pp. 1-1.
- [32] G. Fazio, T. Balčiūnas, Z. Yin, D. Zimin, C. Brahms, J. Travers, and H. J. Wörner, in *The International Conference on Ultrafast Phenomena (UP) 2022*, edited by F. Légaré *et al.* (Optica Publishing Group, Montreal, Quebec, 2022), p. Th4A.38.
- [33] A. L'Huillier, P. Balcou, K. J. Schafer, and K. C. Kulander, in *Coherence Phenomena in Atoms and Molecules in Laser Fields*, edited by A. D. Bandrauk, and S. C. Wallace (Springer US, Boston, MA, 1992), pp. 191-202.
- [34] D. You, R. R. Jones, P. H. Bucksbaum, and D. R. Dykaar, "Generation of high-power sub-single-cycle 500-fs electromagnetic pulses," *Opt. Lett.* **18**, 290-292 (1993).
- [35] H. C. Wu and J. Meyer-ter-Vehn, "Giant half-cycle attosecond pulses," *Nat. Photonics* **6**, 304-307 (2012).
- [36] R. Arkhipov, M. Arkhipov, A. Pakhomov, I. Babushkin, and N. Rosanov, "Half-cycle and unipolar pulses (Topical Review)," *Laser Phys. Lett.* **19**, 043001 (2022).
- [37] N. Rosanov, "Unipolar pulse of an electromagnetic field with uniform motion of a charge in a vacuum," *Phys. Usp.* **193**, 1127-1133 (2023).

- [38] J. R. Bettis, A. H. Guenther, and R. A. House, "Refractive-index dependence of pulsed-laser-induced damage," *Opt. Lett.* **4**, 256-258 (1979).
- [39] C. You, S. Dai, P. Zhang, Y. Xu, Y. Wang, D. Xu, and R. Wang, "Mid-infrared femtosecond laser-induced damages in As₂S₃ and As₂Se₃ chalcogenide glasses," *Sci. Rep.* **7**, 6497 (2017).
- [40] M. Thévenet, A. Leblanc, S. Kahaly, H. Vincenti, A. Vernier, F. Quéré, and J. Faure, "Vacuum laser acceleration of relativistic electrons using plasma mirror injectors," *Nat. Phys.* **12**, 355-360 (2016).
- [41] Y. Morimoto, "Attosecond electron-beam technology: a review of recent progress," *Microscopy* **72**, 2-17 (2023).
- [42] H. Y. Kim, M. Garg, S. Mandal, L. Seiffert, T. Fennel, and E. Goulielmakis, "Attosecond field emission," *Nature* **613**, 662-666 (2023).
- [43] F. J. García de Abajo and C. Ropers, "Spatiotemporal electron beam focusing through parallel interactions with shaped optical fields," *Phys. Rev. Lett.* **130**, 246901 (2023).
- [44] R. J. L. Timmis *et al.*, "Attosecond and nano-Coulomb electron bunches via the zero vector potential mechanism," *Sci. Rep.* **14**, 10805 (2024).
- [45] E. Migal, A. Pushkin, B. Bravy, V. Gordienko, N. Minaev, A. Sirotkin, and F. Potemkin, "3.5-mJ 150-fs Fe:ZnSe hybrid mid-IR femtosecond laser at 4.4 μ m for driving extreme nonlinear optics," *Opt. Lett.* **44**, 2550-2553 (2019).
- [46] O. Uteza, B. Bussière, F. Canova, J. P. Chambaret, P. Delaporte, T. Itina, and M. Sentis, "Laser-induced damage threshold of sapphire in nanosecond, picosecond and femtosecond regimes," *Appl. Surf. Sci.* **254**, 799-803 (2007).
- [47] Y. R. Shen, *Principles of Nonlinear Optics* (Wiley, New York, 1984).
- [48] P. M. Paul, E. S. Toma, P. Breger, G. Mullot, F. Augé, P. Balcou, H. G. Muller, and P. Agostini, "Observation of a train of attosecond pulses from High Harmonic Generation," *Science* **292**, 1689-1692 (2001).
- [49] J. Liang *et al.*, "Attosecond-resolved non-dipole photoionization dynamics," *Nat. Photonics* **18**, 311-317 (2024).

Supplemental Material

Deep-sub-cycle ultrafast optical pulses

Hongliang Dang,¹⁺ Jiaxin Gao,¹⁺ Hao Wu,¹ Xin Guo,¹ Y. R. Shen,² Limin Tong^{1,*}

¹*Interdisciplinary Center for Quantum Information, New Cornerstone Science Laboratory, State Key Laboratory of Extreme Photonics and Instrumentation, College of Optical Science and Engineering, Zhejiang University, Hangzhou 310027, China*

²*Physics Department, University of California at Berkeley, Berkeley, California 94720, USA*

⁺ These authors contribute equally.

* Corresponding authors: phytong@zju.edu.cn

Notations

This work involves the transformation of variables between two coordinate systems — the E. R. frame (electros at rest frame) and the Lab frame (i.e., the stationary observer frame). We denote that in the E. R. frame with a superscript ‘’’, and that in the Lab frame without superscript.

Table 1 gives a list of notations involved in this work.

Table 1. Notations

<u>Coordinate</u>	
ϕ	incident angle in the Lab frame
ϕ'	incident angle in the E. R. frame
θ	scattered angle of the ICS photon in the Lab frame
θ'	scattered angle of the ICS photon in the E. R. frame
Ω	solid angle
ψ	azimuthal angle at the observing plane (i.e., the receiving surface)
x	x coordinate, the direction of the driving optical field propagation

y	y coordinate, the direction of the electric field of the driving optical field in the nano-slit
z	z coordinate, the direction of the electron incidence
$\hat{\mathbf{r}}$	the unit vector pointing from the electron to the observer
r	distance between the electron and the observer
t_g	the moment when the ICS photon is generated in the Lab frame
t	the moment when the ICS photon reaches the observer in the Lab frame

Driving optical field

E_0	photon energy
ν_0	optical frequency
T_{c0}	oscillation period
λ_0	wavelength
τ_0	pulse width
N_0	photon number
E_{p0}	pulse energy
$\mathbf{E}_{\text{driving}}$	electric field of the driving optical field
A_0	amplitude
A_{0N}	normalized amplitude
φ	phase
$g(t_g)$	t_g -dependent envelope
$\mathbf{B}_{\text{driving}}$	magnetic field of the driving field
w	slit width of the nano-slit structure
P_{mode}	average mode power, i.e., $P_{\text{mode}} = E_{p0}/\tau_0$
$\mathbf{S}(\mathbf{z}, \mathbf{y})$	Poynting vector along the propagation direction
$P(z)$	z -dependent power density distribution, i.e., $P(z) = \int_{-w/2}^{w/2} \mathbf{S}(\mathbf{z}, \mathbf{y}) d\mathbf{y} / w$
$F(z)$	photon flux, i.e., $F(z) = N_0 \cdot P(z) / (P_{\text{mode}} \cdot \tau_0)$
FWHM_S	spatial FWHM of the intensity distribution along the z -axis

Incident electron/electron bunch

E_e	electron energy
V_e	electron speed
β	normalized V_e over c , i.e., $\beta = V_e/c$
γ	Lorentz factor, i.e., $\gamma = \sqrt{1/(1 - \beta^2)}$
τ_e	pulse width of the electron bunch
N_e	electron number

ICS pulse

E_{SP}	photon energy
ν	optical frequency
T_{c1}	oscillation period
λ_1	wavelength
N_{SP}	photon number
ν_{peak}	peak frequency
T_{peak}	oscillation period at the peak frequency
τ_1/FWHM_T	pulse width/temporal FWHM
$n(t, \theta)$	ICS photon number received at time t and angle θ
$n(t)$	ICS photon number received at time t , i.e., $n(t) = \int n(t, \theta) d\theta$
$I(t, \theta)$	ICS pulse intensity received at time t and angle θ , i.e., $I(t, \theta) = n(t, \theta) \cdot h\nu$
$I(t)$	ICS pulse intensity received at time t , i.e., $I(t) = \int I(t, \theta) d\theta$
$E(t, \theta)$	electric field of the ICS pulse at time t and angle θ
$E(t)$	electric field of the ICS pulse at time t , i.e., $E(t) = \int E(t, \theta) d\theta$
$E(\nu)$	Fourier spectrum of $E(t)$

Constants

c	speed of light
h	Planck constant
σ_T	Thomson scattering cross-section

e	elementary charge
m_0	electron mass
ε_0	vacuum dielectric constant
μ_0	vacuum permeability

Degree of temporal confinement

ζ	temporal confinement factor
---------	-----------------------------

The remaining unlabeled notations will be further explained in the text.

I. Inverse Compton Scattering (ICS)

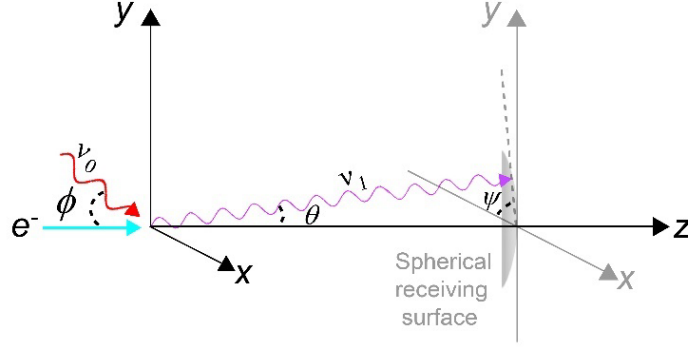


Fig. S1. Inverse Compton scattering of a photon (red arrow line) and an electron (cyan arrow line) colliding with each other on their motion trajectories. The scattered photon (purple arrow line) will be collected at a spherical receiving surface centered around the original point of $x=y=z=0$, with an angle θ determined by Equation (2).

As shown in Fig.S1, for an electron (energy of E_e , speed of V_e) moving along the z-axis, assuming that the incident angle and the scattering angle of a photon (energy of E_0 and wavelength of λ_0) are ϕ and θ in the Lab frame, and ϕ' and θ' in the E. R. frame, respectively. Then, in the Lab frame, we have [1]

1. Energy of scattered photons

$$E_{SP} = E_0 \frac{1 - \beta \cos(\phi)}{1 - \beta \cos(\theta)} , \quad (1)$$

where $\beta = V_e/c$.

In this work, $\phi = 90^\circ$, therefore

$$E_{SP} = \frac{E_0}{1 - \beta \cos(\theta)} ,$$

and the wavelength of the scattered photons

$$\lambda_1 = \lambda_0 \cdot (1 - \beta \cos \theta).$$

2. The range of the scattering angle

$$\sin \theta \in \left[-\frac{1}{\gamma}, \frac{1}{\gamma} \right] , \quad (2)$$

where the Lorentz factor $\gamma = [1/(1 - \beta^2)]^{1/2}$.

II. Time compression effect

Time compression effect is well-known in e.g., synchrotron radiation [2] for an electron moving

with relativistic velocity towards the observer. Since the electron and its radiation travel with comparable velocities, the radiation field generated by the electron over a relatively long time (t_g) is received by the observer within a shorter time interval (t), with

$$t = t_g(1 - \beta \cos \theta) . \quad (3)$$

III. Electron incidence and field intensity distribution of the nano-slit mode

As shown in Fig.S2, in the nano-slit of a coupled nanowire pair (CNP), although the field confinement in the y-direction (~ 20 nm) is tighter than that in the z-direction (~ 77 nm), to avoid the absorption of the electron by the CdS material when it flying through, here we assume that the electron flies through the nano-slit along the z-direction (the white dashed line arrow) and interacts with the optical driving field all the way in the air or vacuum, without touching the edges of the nano-slit.

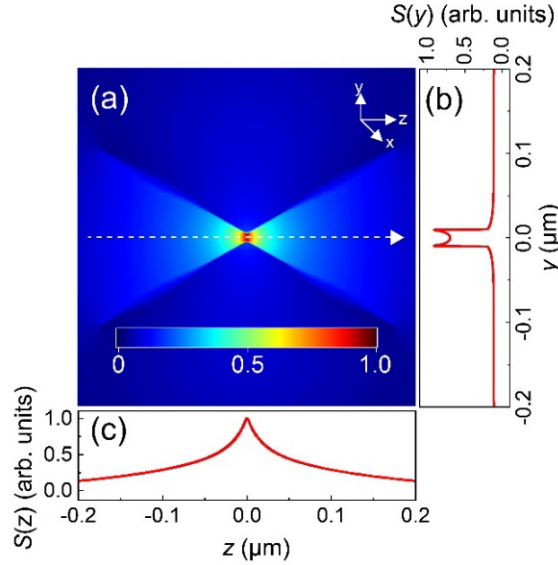


Fig. S2. Calculated Poynting vector of the nano-slit mode in a CNP constructed with two identical hexagonal CdS nanowires with a diameter of 500 nm, a slit width of 20 nm, and a wavelength of $1.8 \mu\text{m}$. (a) 2-dimensional Poynting vector $|S(y, z)|$ in the y - z plane. (b,c) 1-dimensional Poynting vector $S(y) = |S(y, z=0)|$ and $S(z) = |S(y=0, z)|$ along y - and z -axis centrosymmetric lines, respectively. The results are calculated with the finite element method (COMSOL Multiphysics®).

IV. Number of scattered photons in the ICS

Assuming that the optical driving field (i.e., a nano-slit-waveguide mode of a CNP structure [3]) is generated by a femtosecond pulse with a pulse width of τ_0 , a pulse energy of E_{p0} , and a central frequency

of ν_0 , the total number of photons contained in a single-pulse driving field is

$$N_0 = \frac{E_{p0}}{h\nu_0} \quad (4)$$

where h is the Planck constant.

Assuming that the average mode power is $P_{\text{mode}} = E_{p0}/\tau_0$, and the Poynting vector at an arbitrary point is $\mathbf{S}(z, y)$, the number density of the scattered photons along z -direction, $n(z)$, can be obtained in the following cases [4]

1. Single-electron incidence

Assuming that the electron flies through the nano-slit along the central axis (i.e., z -axis) with $y=0$, consider an infinitesimal area $\Sigma = \delta_y \cdot \delta_z$ at the position \mathbf{z} , the power density of the optical driving field on Σ is

$$P(z) = \int_{-\delta_y/2}^{\delta_y/2} \mathbf{S}(\mathbf{z}, \mathbf{y}) d\mathbf{y} / \delta_y \approx S(z, 0) \quad (5)$$

Therefore, during the transition time of the electron δ_t , the number of photons passing through Σ per unit area (i.e., photon flux) at position z is

$$F(z) = n_0 \cdot \frac{P(z) \cdot \Sigma}{P_{\text{mode}} \cdot \Sigma \cdot \tau_0} \approx \frac{E_{p0}}{h\nu_0} \frac{S(z, 0) \cdot \delta_t}{P_{\text{mode}} \cdot \tau_0} \quad (6)$$

Correspondingly, the number density of scattered photons at position \mathbf{z} is

$$n(z) = F(z) \cdot \sigma_T = \frac{E_{p0}}{h\nu_0} \frac{S(z) \cdot \sigma_T}{P_{\text{mode}} \cdot \tau_0} \delta_t \quad (7)$$

where σ_T is the Thomson scattering cross-section ($\sim 6.65 \times 10^{-29} \text{ m}^2$).

2. Electron-bunch incidence

With a total electron number of N_e , a slit width of w , the photon flux at an infinitesimal area $\Sigma = w \cdot \delta_z$ can be similarly obtained as

$$F(z) = \frac{E_{p0}}{h\nu_0} \frac{\int_{-w/2}^{w/2} S(z, y) dy}{P_{\text{mode}} \cdot \tau_0} \cdot \delta_t, \quad (8)$$

and the number density of scattered photons at position z is obtained as

$$n(z) = N_e \cdot \frac{E_{p0}}{h\nu_0} \frac{\int_{-w/2}^{w/2} S(z, y) dy}{P_{\text{mode}} \cdot \tau_0} \cdot \sigma_T \cdot \delta_t. \quad (9)$$

3. Angular distribution of scattered photons

In this work, we assume the incident angle $\phi = 90^\circ$, then the number density of scattered photons per solid angle is [4]

$$\frac{dn}{d\Omega} = K\chi^2 \left[\frac{1}{2} + \chi(\chi - 1)(1 + \cos 2\psi) \right] , \quad (10)$$

where K is a constant coefficient, $\chi=1/[1+\gamma^2\theta^2]$ and ψ is the azimuthal angle at the observing plane (i.e., the receiving surface). By integrating equation (10) over ψ (ranging from $-\pi$ to π), we obtain a θ -dependent distribution of the scattered photons as

$$f(\theta) = K \cdot \chi^2 [1 + 2 \cdot \chi(\chi - 1)]. \quad (11)$$

V. Temporal pulse waveform at the receiving surface

1. Single-electron incidence

From equation (11), the scattered photons received at time t and angle θ is

$$n(t, \theta) = n(z)f(\theta) , \quad (12)$$

Correspondingly, the pulse intensity at time t and angle θ is

$$I(t, \theta) = n(t, \theta) \cdot h\nu \quad (13)$$

where the frequency of the scattered photon $\nu=\nu_0/(1-\beta\cos\theta)$. Thus, the temporal profile of the pulse received at an arbitrary angle θ can be obtained, as shown in Fig. S3 (using the same parameters as in Fig. 2 in the main text).

Then, by integrating equation (13) over θ , we can obtain the single-electron-incidence pulse width τ_1 (or FWHM_T) by

$$\tau_1 = \int_{-\arcsin(\frac{1}{\gamma})}^{\arcsin(\frac{1}{\gamma})} (1 - \beta\cos\theta) \cdot f(\theta) \cdot \frac{\text{FWHM}_S}{v_e} d\theta . \quad (14)$$

For example, in the case of Fig.2c, the calculated τ_1 is ~ 19 as.

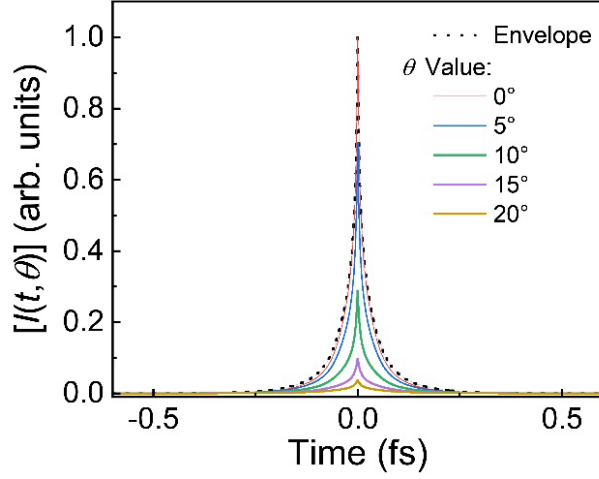


Fig. S3. $I(t, \theta)$ of the single-electron-incidence ICS pulse received at time t and angle θ , calculated with the same parameters as in Fig. 2c.

2. Electron-bunch incidence

With a pulse width of τ_e and a Gaussian profile density distribution (i.e., $n_e = N_e \cdot \exp[-(t_g)^2/\tau_e^2]$, where N_e is the total number of electrons in the bunch), from equations (9) and (12), the number of scattered photons received at time t at angle θ is

$$n(t, \theta) = N_e \cdot n(z) \cdot f(\theta) , \quad (15)$$

here the waveform of the overall pulse is composed of various single-electron-incidence pulse waveforms (here we call them “sub-pulse waveforms”). With the same parameters in Fig.3, we give a close-up view of an overall pulse that is composed of sub-pulse waveforms, as shown in Fig.S4.

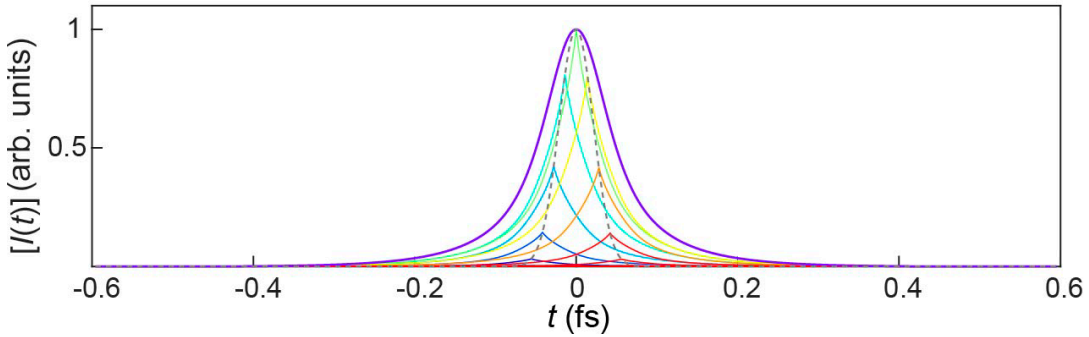


Fig. S4. Waveform of an overall ICS pulse (purple solid line), which is composed of single-electron-incidence sub-pulse waveforms (thin lines with different colors) with a Gaussian-profile temporal distribution (grey dashed line).

VI. Electron's trajectory driven by the nano-slit-mode optical driving field

In a CNP structure, we can selectively support a TE₀-like nano-slit mode with nearly linear polarization along the y direction [3,5,6], with an electric field of

$$\mathbf{E}_{\text{driving}} = A_0 g(t_g) \cos(\varphi) \hat{\mathbf{y}} \quad (16)$$

where A_0 is the amplitude of the nano-slit-mode field, $g(t_g)$ is the amplitude envelope and φ is the phase of the field (i.e., $\varphi = 2\pi\nu_0 t_g$).

Assuming that the incident electron has an initial normalized energy γ (i.e., the Lorentz factor), an initial normalized velocity β , and an initial phase φ of 0, then its energy and momentum satisfy the relativistic kinematic equations [7]

$$\frac{d(\gamma\beta)}{dt} = -\frac{e}{m_0 c} (\mathbf{E}_{\text{driving}} + \mathbf{V}_e \times \mathbf{B}_{\text{driving}}) \quad (17)$$

$$\frac{d\gamma}{dt} = -\frac{e}{m_0 c^2} \mathbf{V}_e \cdot \mathbf{E}_{\text{driving}} \quad (18)$$

where e is the elementary charge of the electron, m_0 is the rest mass of the electron and $\mathbf{B}_{\text{driving}}$ is the magnetic field of the nano-slit-mode optical field. Based on equations (17) and (18), the electron's velocity can be obtained as

$$\begin{cases} \beta_x = \frac{\frac{A_{0N}^2}{2\gamma^2} G_1^2(\varphi)}{1 + \frac{A_{0N}^2}{2\gamma^2} G_1^2(\varphi)} \\ \beta_y = \frac{A_{0N} G_1(\varphi)}{\gamma \left[1 + \frac{A_{0N}^2}{2\gamma^2} G_1^2(\varphi) \right]} \\ \beta_z = \frac{\beta}{1 + \frac{A_{0N}^2}{2\gamma^2} G_1^2(\varphi)} \end{cases} \quad (19)$$

where A_{0N} is the normalized amplitude of the driving field (i.e., $A_{0N} = \frac{eA_0}{m_0 2\pi\nu_0 c}$), and $G_1(\varphi) = -\int_0^\varphi g(\varsigma) \cos\varsigma d\varsigma$.

From equation (18), we can obtain the electron's trajectory

$$\begin{cases} x = \frac{c}{2\pi\nu_0} \frac{A_{0N}^2}{2\gamma^2} \cdot \int_0^\varphi G_1^2(\varsigma) d\varsigma \\ y = \frac{c}{2\pi\nu_0} \frac{A_{0N}}{\gamma} \cdot \int_0^\varphi G_1(\varsigma) d\varsigma \\ z = \frac{c}{2\pi\nu_0} \beta \varphi \end{cases} \quad (20)$$

Based on the above formula, we calculate the trajectory of an incident 2-MeV electron flying through a nano-slit of a CNP structure constructed with two identical sapphire hexagonal prisms (with a diagonal diameter of 1.2 μm , a slit width of 200 nm) at 4.4- μm wavelength (the same parameters used in Fig.3), as shown in Figs. S5a-c. After flying through the nano-slit along the z -direction for $\sim 10 \mu\text{m}$, the electron is slightly deflected in the y -direction for about 40 nm (Fig. S5d), a very slight deviation from its original z -direction. Therefore, the trajectory of the electron can be roughly regarded as a straight line (Figs. S5c-f).

Also, since the transition time of the electron (δ_t) is much shorter than the width of the driving pulse (τ_0), the phase of the driving field is almost unchanged when the electron flying through (Fig. S5a), resulting in a largely unidirectional acceleration and consequently unipolar radiation of the electron.

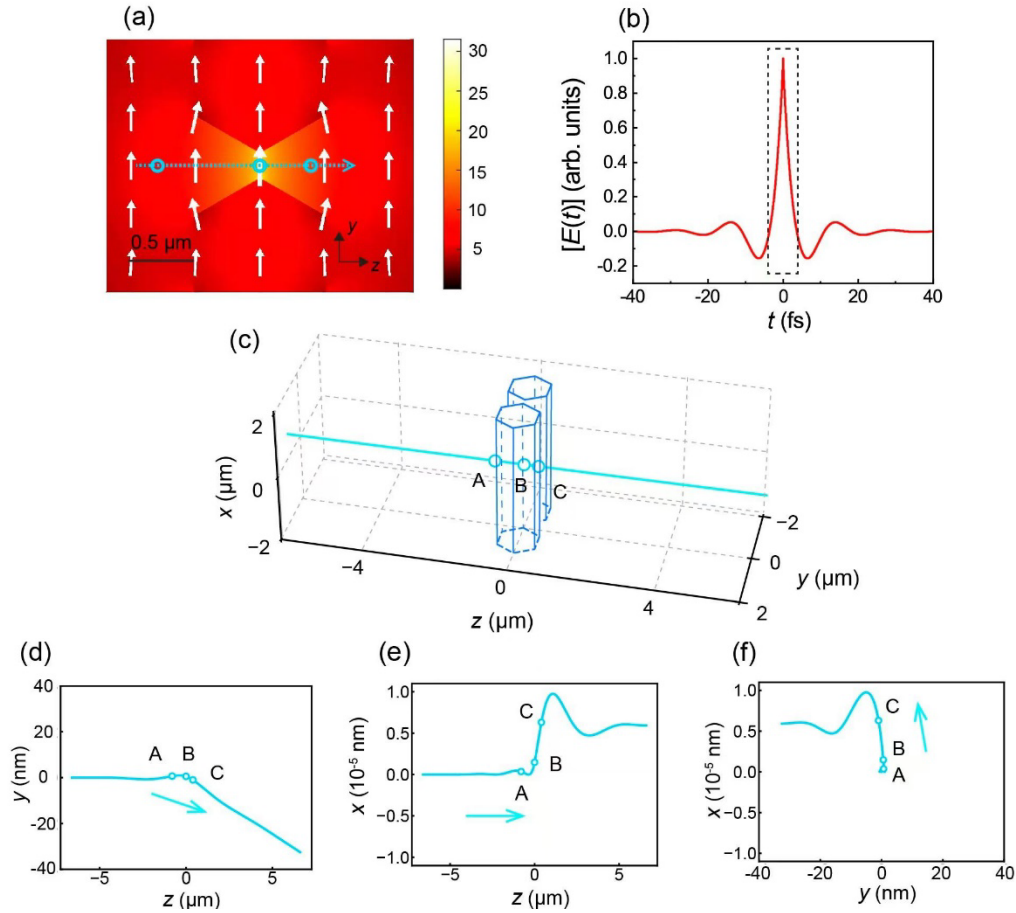


Fig. S5. Calculation of the trajectory of a 2-MeV electron driven by a nano-slit optical field at 4.4- μm wavelength. The nano-slit is constructed with two identical sapphire prisms with a diameter of 1.2 μm and a slit width of 200 nm. (a) Calculated electric field of the optical driving field in the y - z plane. The orientation and size of the white arrow indicate the polarization and amplitude of the local field. The cyan dotted line arrow represents the direction of electron's trajectory, and the cyan circles represent electron's positions at $z = -800 \text{ nm}$, 0 and 400 nm for A, B and C, respectively. (b) $E(t)$ of the nano-slit-mode optical driving field

along z axis, noting that the spatial area in Fig. S5a corresponds to a narrow temporal region (black dashed rectangle). (c) Schematic of the electron flying through the nano-slit. (d-f) Trajectories of the electron at cross-section planes of (d) yz , (e) xz , and (f) xy , respectively.

VII. Electric field and Fourier spectrum at the receiving surface

Following the ICS model, since the phase of the scattered field is inherited from the driving optical field [8], if we assume that the amplitude of the driving field reaches the positive maximum when the electron arrives at the central point of the nano-slit (i.e., $z=0$), in the spatial far field under a plane-wave approximation, the transverse scattered electric field $E_y(t, \theta)$ can be obtained as

$$E_y(t, \theta) = \sqrt{2 \sqrt{\frac{\mu_0}{\epsilon_0}} \cdot I(t, \theta)} e^{i2\pi\nu_0 \left(\frac{t}{1-\beta \cos \theta} \right)}, \quad (21)$$

On the other hand, from classical electrodynamics, the radiation field from an accelerated electron (here the electron is accelerated by the optical driving field) can be obtained as [2]

$$\mathbf{E}_y(\mathbf{t}, \boldsymbol{\theta}) = \frac{e}{4\pi\epsilon_0} \left\{ \frac{\hat{\mathbf{r}} \times [(\hat{\mathbf{r}} - \boldsymbol{\beta}) \times \dot{\boldsymbol{\beta}}]}{cr(1-\hat{\mathbf{r}} \cdot \boldsymbol{\beta})^3} \right\}, \quad (22)$$

where $\hat{\mathbf{r}}$ is the unit vector pointing from the electron to the observer (with r indicating the distance), and $\dot{\boldsymbol{\beta}}$ represents the acceleration of electrons as

$$\dot{\boldsymbol{\beta}} = - \frac{e(\mathbf{E}_{\text{driving}} + \mathbf{V}_e \times \mathbf{B}_{\text{driving}})}{\gamma m_0} \quad (23)$$

To compare the two different models described by equations (21) and (22), using the same parameters in Fig. 3, we calculate the electric field of the scattered/radiated photons and its Fourier spectrum by

$$\begin{cases} \mathbf{E}_y(\mathbf{t}) = \int \mathbf{E}_y(\mathbf{t}, \boldsymbol{\theta}) d\theta \\ E(\nu) = \int_{-\infty}^{\infty} E(t) e^{-j2\pi\nu t} dt \end{cases}, \quad (24)$$

with results given in Fig. S6.

It shows that, the results from the two models agree very well, with the same peak frequency ν_{peak} of ~ 2.55 PHz ($\sim T_{\text{peak}}$ of 0.39 fs).

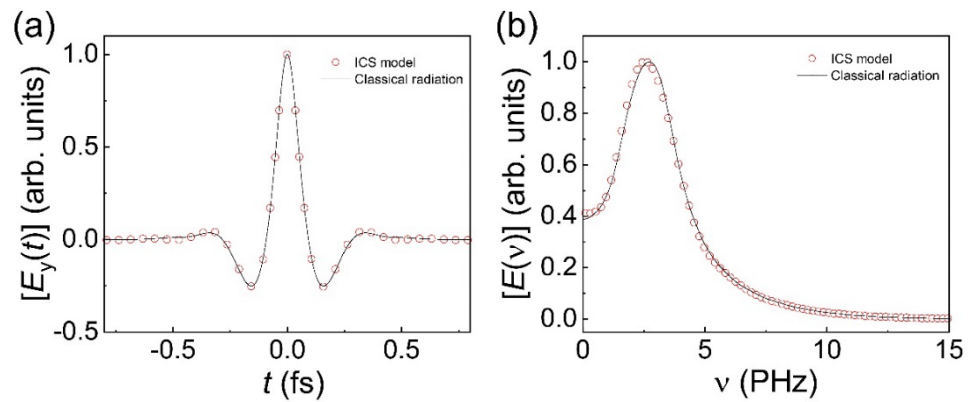


Fig. S6. Comparison of electric fields calculated with ICS model (red circle) and classical radiation model (black solid line). (a) $E_y(t)$, and (b) $E(\nu)$.

VIII. Peak power density around optical damage threshold

The power densities at the center of the optical driving field and the inner surface of the nano-slit are obtained by the numerical calculation using COMSOL. Due to the abrupt refractive-index change at the edge of the nano-slit (i.e., edge of the sapphire prism), in the nano-slit mode, the maximum power density appears at both edges of the nano-slit (as shown in Fig. S7(a)-(d)). To calculate the power density around the edge, a small rectangle of $0.5 \text{ nm} \times 0.5 \text{ nm}$ is taken on the inner edge of the nano-slit (Fig. S7(f)), and the total power density in the small rectangle is approximately regarded as the optical power density at the edge of the nano-slit. When we define a ratio η of the power in the small rectangle to the total power in the entire cross-section area, we obtain $\eta \sim 1 \times 10^{-7}$. Then we use the same parameters in Fig. 3(b) in the main text, with a peak power of the driving laser of $4.4 \times 10^6 \text{ W}$, we obtain a peak power in the small rectangle of $\sim 0.44 \text{ W}$ at the two vertically opposite vertices, corresponding to a power density of $\sim 2 \times 10^{18} \text{ W/m}^2$ at the edge of the nano-slit.

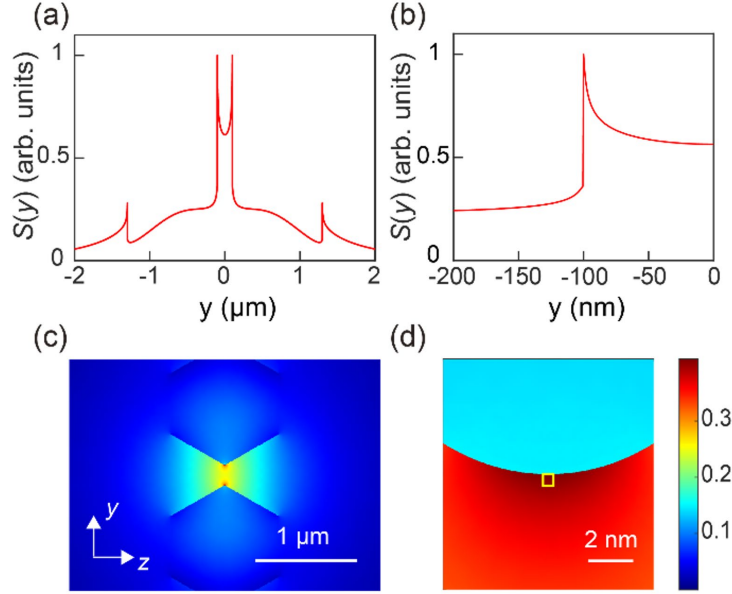


Fig. S7. Derivation of the peak power density at the nano-slit edge of a coupled sapphire prism pair, with a prism diameter of $1.2 \text{ } \mu\text{m}$, a wavelength of $4.4 \text{ } \mu\text{m}$ and a slit width of 200 nm . (a) Poynting vector along y direction. (b) Close-up view of the Poynting vector around the left edge of the nano-slit in (a). (c) Poynting vector of the optical driving optical field in the y - z plane. (d) Close-up view of defining a $0.5 \text{ nm} \times 0.5 \text{ nm}$ rectangle at the vertex of the inner edge of the nano-slit.

IX. Comparison of ζ between different methods

For ease comparison, calculated ζ of this and some previous works on attosecond or sub-cycle pulses are presented in Table 2 and Fig. S8.

Table 2 Experimental parameters and calculated ζ of some previous works on attosecond or sub-cycle pulse generation, based on high harmonic generation (HHG) or pulse coherent synthesis (CS) methods.

Year of publication	Method	λ_0 (nm)	λ_1 (nm)	τ_1 (as)	ζ	References
2001	HHG	750	13.8	650	0.071	[9]
2006	HHG	750	34.5	130	0.885	[10]
2008	HHG	720	15.5	80	0.647	[11]
2011	CS	780	710	2100	1.13	[12]
2012	CS	800	760	3650	0.694	[13]
2012	HHG	750	9.55	67	0.475	[14]
2017	HHG	1800	3.76	53	0.237	[15]
2017	HHG	1800	6.9	43	0.535	[16]
2017	CS	2100	4200	12400	1.13	[17]
2020	CS	800	1400	2800	1.67	[18]
2024	HHG	1064	62	240	0.863	[19]

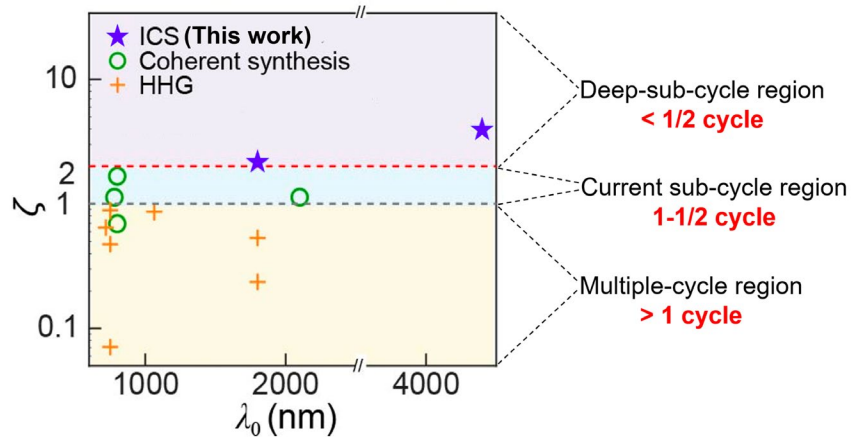


Fig. S8. Calculated ζ of this and some previous works (purple star: ICS green circle: coherent synthesis; orange cross: HHG;). These ICS pulses are generated by a 50-as 2-MeV electron bunch in two sapphire prisms with 0.5- μm diameter, 200-nm slit size (for a 1.8- μm -wavelength driving field) and 1.2- μm diameter, 200-nm slit size (for a 4.4- μm -wavelength driving field), respectively.

X. Temporal evolution and carrier envelope (CE) of the ICS pulse during propagation

After the ICS pulse is generated in the confined optical driving field of the nano-slit, it will propagate continuously within a cone symmetric around the z -axis, followed by the electron pulse. When the spherical receiving surface is close to the center of the nano-slit, e.g., 0.1 mm far away in z -direction, the calculated overall transverse electric field $E_y(t)$ is given in Fig.S9a. The clear asymmetric profile (purple solid line) is caused by the electrostatic field of the moving electron: when the electron passes through the origin at $t=0$ (i.e., $z=0$), viewing from the y -direction, it changes its position from positive to negative (see Fig.S5d), resulting in a sign change of its electrostatic field at the receiving surface (cyan dashed line). Since the receiving distance ($z=100 \mu\text{m}$) is relatively small, this asymmetric-profile field is not negligible, leading to the asymmetric profile of the overall pulse. When the receiving distance increases to $z=1 \text{ mm}$, as shown in Fig.S9b, the amplitude of the electrostatic field (of the electron at $t=0$) at the receiving surface reduces to a negligible level (cyan dashed line), the overall field (purple solid line) is almost the same as the ICS field and becomes quite symmetric. When the receiving distance increases to $z=10 \text{ mm}$, as shown in Fig.S9c, the amplitude of the electrostatic field (of the electron at $t=0$) at the receiving surface is further reduced and completely negligible (cyan dashed line), the overall field (purple solid line) becomes a highly symmetric ICS field.

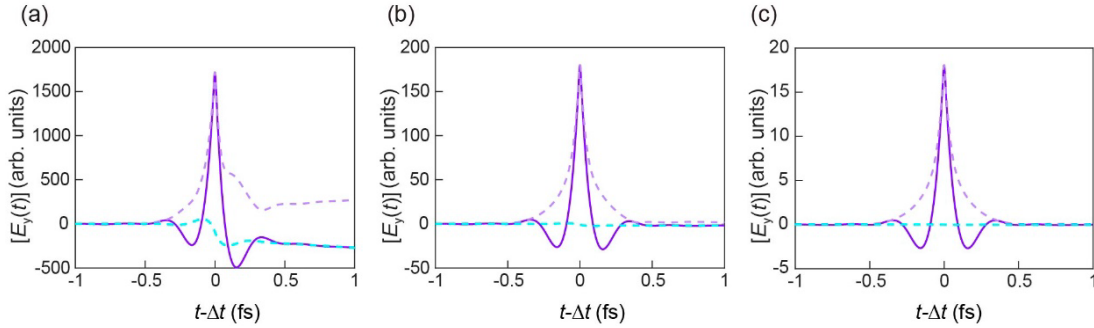


Fig. S9. Temporal evolution and CE of the ICS pulse during propagation. Here $E_y(t)$ is the calculated overall transverse electric field (purple solid line) combining both the ICS pulse and the fluctuation of electrostatic field of the electron in the y -axis (cyan dashed line), with a position of the center of the receiving surface (z) assumed to be (a) $z=0.1 \text{ mm}$, (b) $z=1 \text{ mm}$, and (c) $z=10 \text{ mm}$. The carrier envelope of $E_y(t)$ is also given (purple dashed line). $\Delta t = \Delta z/c$ is the pulse propagation time from the nano-slit center (i.e., $z=0$) to the receiving surface.

The evolution of the carrier envelope (CE) of the ICS pulse is also given in Fig.S9 (purple dashed line). When $z=0.1 \text{ mm}$, the CE is asymmetric due to the influence of the electrostatic field (Fig.S9a); when $z=1 \text{ mm}$, the CE becomes symmetric (Fig.S9b) and will not change when the pulse propagates further to $z=10 \text{ mm}$ (Fig.S9c), showing the stable carrier-envelope phase (CEP) of the ICS pulse during its propagation in free space.

References

- [1] G. Ghisellini, *Radiative Processes in High Energy Astrophysics*, Vol. 873, Springer International Publishing, Heidelberg, 2013.
- [2] A. Hofmann, *The Physics of Synchrotron Radiation*, Cambridge University Press, Cambridge, 2004.
- [3] L. Yang, Z. K. Zhou, H. Wu, H. L. Dang, Y. X. Yang, J. X. Gao, X. Guo, P. Wang, and L. M. Tong, “Generating a sub-nanometer-confined optical field in a nanoslit waveguiding mode”, *Adv. Photonics* **5**, 046003 (2023).
- [4] R. W. Schoenlein, W. P. Leemans, A. H. Chin, P. Volfbeyn, T. E. Glover, P. Balling, M. Zolotarev, K.-J. Kim, S. Chattopadhyay, and C. V. Shank, “Femtosecond X-ray pulses at 0.4 Å generated by 90° Thomson scattering: a tool for probing the structural dynamics of materials”, *Science* **274**, 236-238 (1996).
- [5] H. Wu, L. Yang, P. Z. Xu, J. Gong, X. Guo, P. Wang, and L. M. Tong, “Photonic nanolaser with extreme optical field confinement,” *Phys. Rev. Lett.* **129**, 013902 (2022).
- [6] Y. X. Yang, J. X. Gao, H. Wu, Z. K. Zhou, L. Yang, X. Guo, P. Wang, and L. M. Tong, “Generating a nanoscale blade-like optical field in a coupled nanofiber pair”, *Photonics Res.* **12**, 154-162 (2024).
- [7] K. Lee, Y. H. Cha, M. S. Shin, B. H. Kim, and D. Kim, “Relativistic nonlinear Thomson scattering as attosecond x-ray source,” *Phys. Rev. E* **67**, 026502 (2003).
- [8] A. L’Huillier, P. Balcou, K. J. Schafer, and K. C. Kulander, *Coherence in Strong Field Harmonic Generation*, in *Coherence Phenomena in Atoms and Molecules in Laser Fields*, edited by A. D. Bandrauk and S. C. Wallace, Vol. 287, Springer US, Boston, MA, 1992, pp. 191–202.
- [9] M. Hentschel, R. Kienberger, C. Spielmann, G. A. Reider, N. Milosevic, T. Brabec, P. Corkum, U. Heinzmann, M. Drescher, and F. Krausz, “Attosecond metrology,” *Nature* **414**, 509-513 (2001).
- [10] G. Sansone E. Benedetti, F. Calegari, C. Vozzi, L. Avaldi, R. Flammini, L. Poletto, P. Villoresi, C. Altucci, R. Velotta, S. Stagira, S. De Silvestri, and M. Nisoli, “Isolated single-cycle attosecond pulses,” *Science* **314**, 443-446 (2006).
- [11] E. Goulielmakis, M. Schultze, M. Hofstetter, V. S. Yakovlev, J. Gagnon, M. Uiberacker, A. L. Aquila, E. M. Gullikson, D. T. Attwood, R. Kienberger, F. Krausz, and U. Kleineberg, “Single-cycle nonlinear optics,” *Science* **320**, 1614-1617 (2008).
- [12] A. Wirth, M. Th. Hassan, I. Grguraš, J. Gagnon, A. Moulet, T. T. Luu, S. Pabst, R. Santra, Z. A. Alahmed, A. M. Azzeer, V. S. Yakovlev, V. Pervak, F. Krausz, and E. Goulielmakis “Synthesized light transients,” *Science* **334**, 195-200 (2011).
- [13] C. Manzoni, S.-W. Huang, G. Cirmi, P. Farinello, J. Moses, F. X. Kärtner, and G. Cerullo, “Coherent synthesis of ultra-broadband optical parametric amplifiers,” *Opt. Lett.* **37**, 1880-1882 (2012).
- [14] K. Zhao, Q. Zhang, M. Chini, Y. Wu, X. W. Wang, and Z. H. Chang, “Tailoring a 67 attosecond pulse through advantageous phase-mismatch,” *Opt. Lett.* **37**, 3891-3893 (2012).
- [15] J. Li, X. M. Ren, Y. C. Yin, K. Zhao, A. Chew, Y. Cheng, E. Cunningham, Y. Wang, S. Y. Hu, Y. Wu, M. Chini and Z. H. Chang, “53-attosecond X-ray pulses reach the carbon K-Edge,” *Nat. Commun.* **8**, 186 (2017).

- [16] T. Gaumnitz, A. Jain, Y. Pertot, M. Huppert, I. Jordan, F. Ardana-Lamas, and H. J. Wörner, “Streaking of 43-attosecond soft-X-ray pulses generated by a passively CEP-stable mid-infrared driver,” *Opt. Express* **25**, 27506 (2017).
- [17] H. Liang, P. Krogen, Z. Wang, H. Park, T. Kroh, K. Zawilski, P. Schunemann, J. Moses, L. F. DiMauro, F. X. Kärtner, and K. Hong, “High-energy mid-infrared sub-cycle pulse synthesis from a parametric amplifier,” *Nat. Commun.* **8**, 141 (2017).
- [18] G. M. Rossi, R. E. Mainz, Y. D. Yang, F. Scheiba, M. A. Silva-Toledo, S. Chia, P. D. Keathley, S. B. Fang, O. D. Mücke, C. Manzoni, G. Cerullo, G. Cirimi, and F. X. Kärtner, “Sub-cycle millijoule-level parametric waveform synthesizer for attosecond science,” *Nat. Photonics* **14**, 629-635 (2020).
- [19] M. Kretschmar, E. Svirplys, M. Volkov, T. Witting, T. Nagy, M. J. J. Vrakking, and B. Schütte, “Compact realization of all-attosecond pump-probe spectroscopy,” *Sci. Adv.* **10**, eadk9605 (2024).